

# EnKF assimilation of storm-scale, mobile Doppler radar data for high-resolution analyses of a weakly tornadic supercell

Robin L. Tanamachi<sup>1</sup>, Ming Xue<sup>1</sup>, Youngsun Jung<sup>1</sup>, Keith A. Brewster<sup>1</sup>, Michael I. Biggerstaff<sup>2</sup>

<sup>1</sup>Center for Analysis and Prediction of Storms, University of Oklahoma, Norman, Oklahoma, U.S.A., [rtanamachi@ou.edu](mailto:rtanamachi@ou.edu)

<sup>2</sup>School of Meteorology, University of Oklahoma, Norman, Oklahoma

(Dated: 18 June 2012)



Robin Tanamachi  
[rtanamachi@ou.edu](mailto:rtanamachi@ou.edu)

## 1. Introduction

Recent efforts to include mobile and other non-standard ground-based radar data in ensemble analyses of severe convective storms have yielded promising results (e.g., Marquis et al. 2010; Snook et al. 2011; Tanamachi et al. 2012). During Project VORTEX2 (Wurman et al. 2010), the field phase of which occurred in spring 2009 and spring 2010, coordinated mobile Doppler radar deployments resulted in data collection in a variety of severe convective storms, including supercells and quasi-linear convective systems. This body of data provides a unique opportunity to verify wind retrievals against Doppler velocities recorded by other high-resolution radars.

In this study, we assimilated data from C-band Shared Mobile Atmospheric Research and Teaching Radars (SMART-R; Biggerstaff et al. 2005), as well as other radars, into the Advanced Regional Prediction System (ARPS; Xue et al. 2000) to analyze the 26 May 2010 Prospect Valley, Colorado supercell (hereafter “the Prospect Valley storm”; Fig. 1). We evaluate these analyses by subjectively locating storm features and by comparing synthetic Doppler velocities produced from the analyzed model states to those observed by other radars. In contrast to most earlier EnKF studies of severe convective storms initialized in a horizontally homogeneous environment, we use horizontally inhomogeneous initial conditions (background), similar to some recent studies (Stensrud and Gao 2010; Snook et al. 2011; Jung et al. 2012).

We selected the isolated, weakly tornadic Prospect Valley storm for study because radar coverage was exceptionally good. Because of its slow east-northeastward movement over relatively flat terrain, this storm was easily targeted by VORTEX2 teams, many of which collected over an hour of data prior to the occurrence of several weak, tornado-like vortices (TLVs) between 2217 and 2246 UTC. Near-continuous reflectivity ( $Z$ ) and Doppler velocity ( $V_r$ ) observations were made in the Prospect Valley storm by no fewer than 10 ground-based mobile Doppler radars. In addition, WSR-88Ds at Denver, Colorado (KFTG), Pueblo, Colorado (KPUX), and Cheyenne, Wyoming (KCYS) also recorded data in this storm. These data sets provide ample opportunity both for assimilation and for independent verification.

## 2. VORTEX2 radar data collection in the Prospect Valley storm

The first echoes of the developing Prospect Valley supercell appeared over eastern Denver in KFTG reflectivity data around 1845 UTC. At 1920 UTC, the storm split into left- and right-moving supercells. The left-moving supercell raced away to the north. The right-moving supercell, the Prospect Valley storm, moved slowly (at 5 to 6 m s<sup>-1</sup>) toward the northeast along U. S. Interstate Highway 76 (I-76). The Prospect Valley storm remained fairly isolated until it dissipated at 0300 UTC on 27 May.

Between 1930 and 2110 UTC, storm spotters reported at least four separate tornadoes from this storm as it tracked over Adams County and into southern Weld County, prompting a tornado warning from the U.S. National Weather Service office in Denver, Colorado. However, there were no tornado reports during VORTEX2 operations (2150 – 0041 UTC).

VORTEX2 initially targeted the Prospect Valley storm north of Denver International Airport, near Hudson, Colorado, at 2100 UTC. Teams converged on the storm in southern Weld County, and began collecting coordinated data sets at 2150 UTC. The slow storm motion and relatively flat terrain east of Prospect Valley made the storm an easy target for most VORTEX2 platforms. Many teams collected up to an hour of continuous data, including dual-Doppler data collected by the

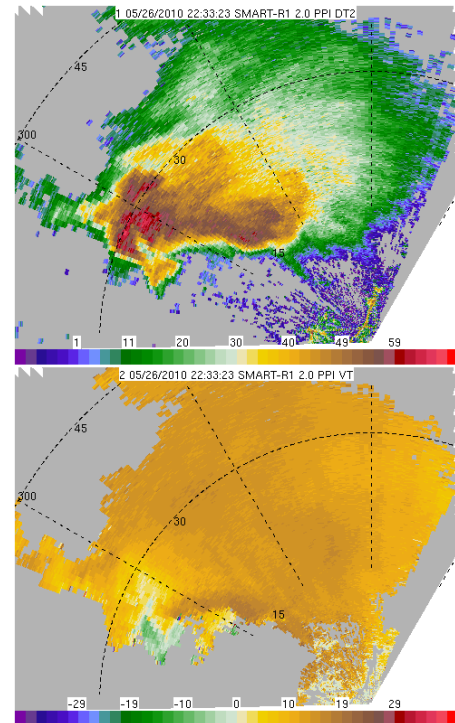


Fig. 1. (a) Reflectivity (in dBZ) and (b) Doppler velocity (in m s<sup>-1</sup>) in the Prospect Valley storm as seen by the first of two SMART-Rs at 2233 UTC on 26 May 2010 at an elevation angle of 2.0°. Range rings are every 15 km.

two SMART-Rs (SR1 and SR2; 2227-2324 UTC, in 3-min volumes). Operations ended at 0041 UTC on 27 May, when the Prospect Valley storm entered an area with a poor road network.

This case is recorded in VORTEX2 summaries (e.g., Wurman *et al.* 2010) as a nontornadic supercell because no *visible* tornado funnel was documented. However, high-resolution Doppler radar observations from the tornado-scale UMass W-band and Texas Tech University Ka-band radars clearly show a succession of TLVs, defined as Doppler velocity couplets with weak-echo holes (WEHs), between about 2217 and 2246 UTC. Detailed GBVTD analyses of one of these TLVs are reported separately in this volume (paper 377).

### 3. EnKF experiment setup

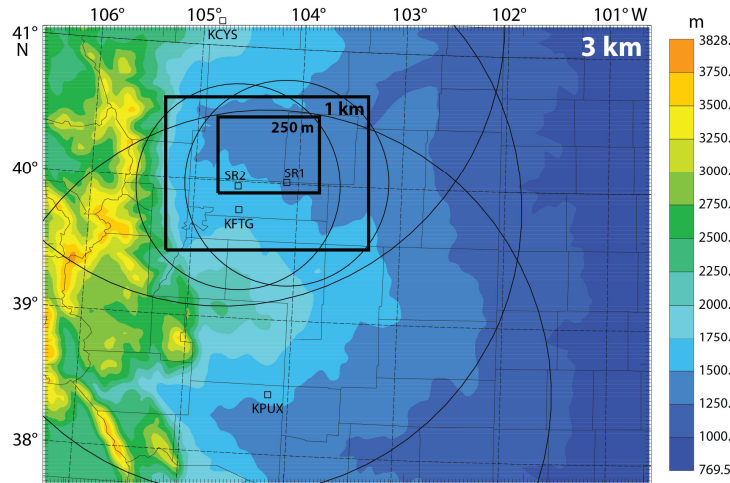


Fig. 2. Nested experiment domain in northeast Colorado. Colored shadings represent terrain height. Maximum range rings are shown for each radar.

Our experiment commenced at 1800 UTC on 26 May when a 3 km ensemble was launched from a perturbed 1800 UTC operational NAM analysis. The experiment continued through 0000 UTC on 27 May, encompassing the time of the VORTEX2 operations and data collection. To populate the initial (1800 UTC) ensemble, mesoscale perturbations with horizontal (vertical) length scales of 17 km (1.7 km) were added to the  $u$ ,  $v$ , and  $\theta$  fields on the 3 km grid. The  $u$  and  $v$  ( $\theta$ ) perturbations were created by applying recursive filters (Hayden and Purser 1995) to random Gaussian perturbations with standard deviations of  $0.5 \text{ m s}^{-1}$  (0.25 K). Additional, smaller-scale perturbations were added at 1920 UTC in areas of ongoing convection.  $Z$  and  $V_r$  observations from KCYS and KPUX were then assimilated on the 3 km grid in 5-min cycles starting at 1930 UTC. On the nested 1 km (250 m) grid, KFTG (SR1)  $Z$  and  $V_r$  observations were assimilated in 5-min (3-min cycles) starting at 2100 UTC (2227 UTC), with each one-way nested grid inheriting initial analysis background and lateral boundary conditions from the next coarser one. The assumed observation errors for  $Z$  and  $V_r$  were 5 dBZ and  $2 \text{ m s}^{-1}$ , respectively. Ensemble spread was maintained via a combination of additive noise (Caya *et al.* 2005) and multiplicative inflation (Anderson 2001). Our experiment setup is summarized in Fig. 3.

### 4. Results

Assimilation of the KCYS and KPUX  $Z$  and  $V_r$  observations on the 3 km grid established the large-scale features of the Prospect Valley storm and its environment. Assimilation of  $Z$  and  $V_r$  from KFTG and SR1 on the 1 km and 250 m grid, respectively, resulted in more detailed structures of the Prospect Valley storm. All ensemble members had an isolated supercell corresponding to the Prospect Valley storm, with most spurious convection in the surrounding area effectively suppressed (Fig. 4) via assimilation of reflectivity data in precipitation-free regions. We focus on results from the 250 m grid, where SR1 data were assimilated, for the remainder of this discussion.

An ensemble Kalman filter package has been developed and continually enhanced within the ARPS modeling framework (ARPSEnKF; Tong and Xue 2005; Xue *et al.* 2006). In order to capture the impact of the mesoscale environment on the limited domain over which we assimilated storm-scale radar data, we employed a triply-nested experiment domain. The outermost grid, with 3 km horizontal grid spacing, was centered on the northeast quadrant of Colorado in order to cover the source region of low-level inflow air (eastern Colorado; Fig. 2). The western portion of this outer domain contains some of the more complex terrain of the Rocky Mountains; the eastern portion slopes gently downward toward the east, covering portions of the High Plains in Kansas and Nebraska. The nested 1 km grid and 250 m grid inherited horizontally interpolated terrain from the 3 km grid and 1 km grid, respectively. All three grids have the same stretched vertical terrain-following model levels; the near-surface vertical grid spacing is 50 m.

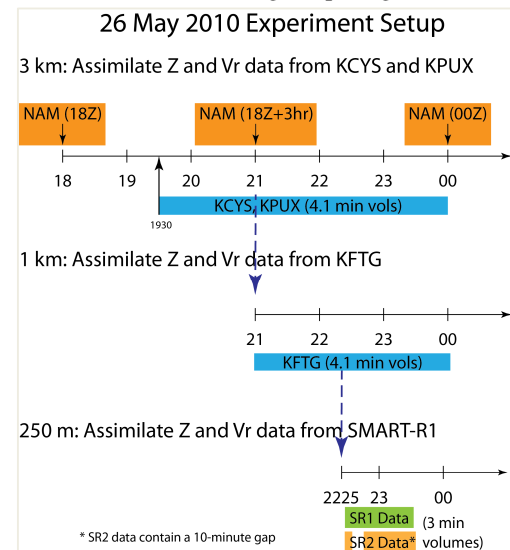


Fig. 3. Flow diagram for our experiment.

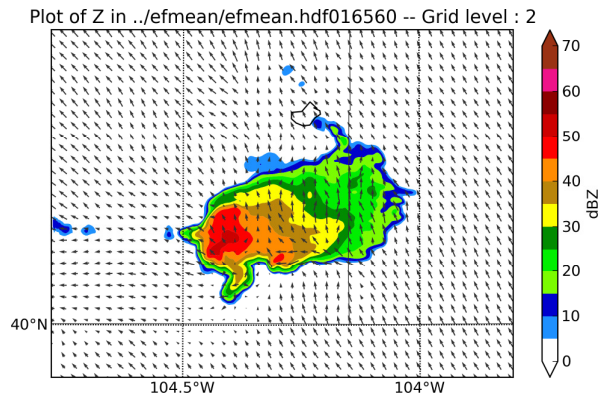


Fig. 4. Prior ensemble mean reflectivity (in dBZ) and storm-relative wind vectors (in  $m s^{-1}$ , plotted every 4 km) at 50 m AGL on the 250 m domain at 2236 UTC.

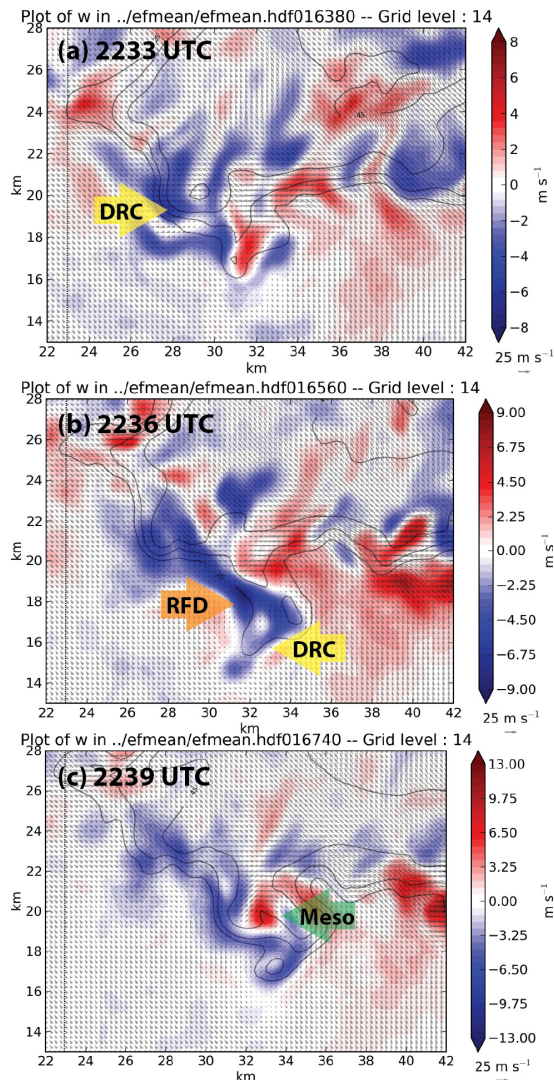


Fig. 5. Prior ensemble mean vertical velocity (colored shading in  $m s^{-1}$ ), reflectivity (black contours of 25, 35, and 45 dBZ) and storm-relative wind vectors (in  $m s^{-1}$ , plotted every 250 m) at 1 km AGL at (a) 2233 UTC, (b) 2236 UTC, and (c) 2239 UTC. The view is enlarged relative to that in Fig. 4.

Of primary interest is the time period (2233 – 2244 UTC) when the most intense TLV was recorded by the tornado-scale radars. During that period, multiple descending reflectivity cores (DRCs) (Rasmussen et al. 2006) were visually confirmed on the rearward (with respect to storm motion) side of the hook echo. One of these DRCs descended past the 1 km AGL level at roughly 2233 UTC, resulting in a southward extension of the reflectivity hook at 2236 UTC. This DRC was followed closely by a rear-flank downdraft (RFD) surge that wrapped around the reflectivity appendage between 2236 and 2239 UTC, during which time the maximum vorticity near the tip of the hook at 1 km AGL increased from  $0.03 s^{-1}$  to  $0.12 s^{-1}$ . The DRC and RFD are reflected in the 1 km AGL reflectivity and w-fields in the 3-min ensemble mean forecast (Fig. 5).

## 5. Trajectory analyses

During each forecast cycle, the model state was recorded every 5 seconds in order to enable accurate backwards trajectory calculations in the zone of convergence around the mesocyclone. For each member, we initialized a cluster of nine, 3 min long, backward trajectories (covering the forecast cycle preceding the peak intensity of TLV #4, 0233-0236 UTC), one at a vorticity maximum along the inner edge of the hook echo (thought to reflect the ensemble member realization of TLV #4) and eight more arrayed in a circle of 150 m radius surrounding the vorticity maximum (to account for uncertainty in its location). One set of trajectories was initialized from 50 m AGL (the model level closest to the surface), and the other from 1 km AGL. An example of the latter is shown in Fig. 6.

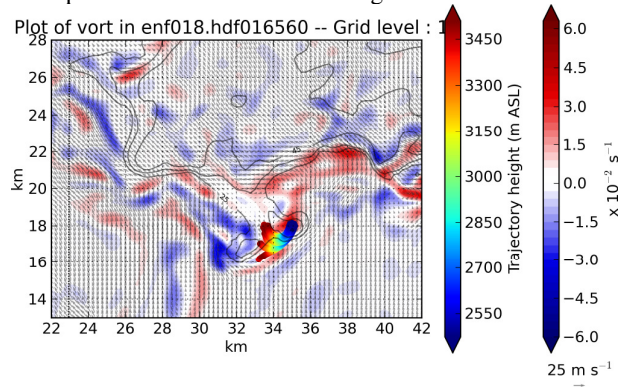


Fig. 6. Ensemble member 18 forecast vorticity (in  $10^{-2} s^{-1}$ , filled color contours) and storm-relative wind vectors (in  $m s^{-1}$ , plotted every 250 m) at 1 km AGL on the 250 m domain at 2236 UTC. Nine backward trajectories (curves color-coded by height) are overlaid.

The resulting ensemble of trajectory sets is shown in Fig. 7 plotted relative to the vorticity maximum. Backward trajectories initialized from 50 m AGL originate from all directions around the vorticity maximum, but a majority come from the inflow sector. In the vertical, most trajectories remained within  $\pm 20$  m of their terminuses for the three preceding minutes. In contrast, air flow entering the vorticity maximum at 1 km AGL (taken as a proxy for the low-level mesocyclone) originated from two principal sources: (1) descending into the vortex from the west or

northwest (77%), or (2) ascending into the vortex from the inflow sector (23%).

Backwards trajectories from 2236 UTC

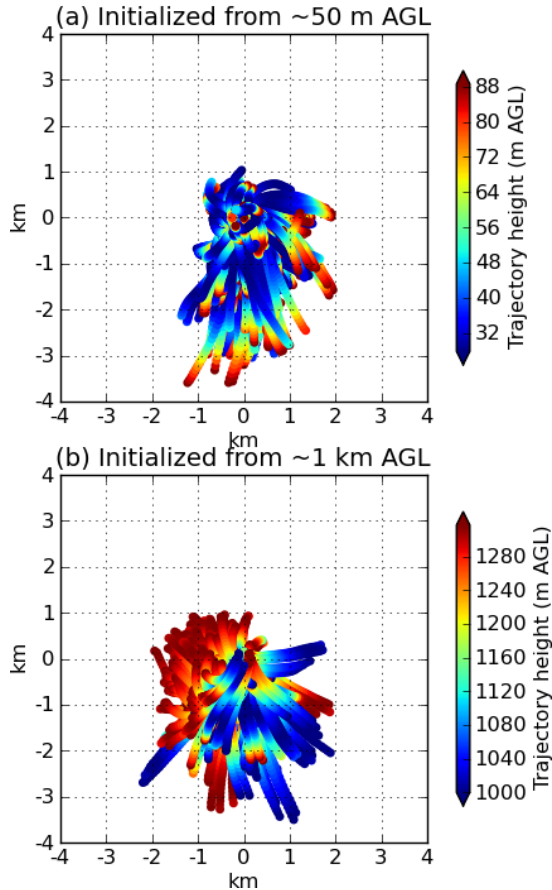


Fig. 7. Backwards parcel trajectories initialized from vorticity maxima in the hook echo at 2236 UTC from (a) 50 m AGL and (b) 1 km AGL. All trajectories are plotted relative to their point of initiation; hence, they all terminate near the origin.

It appears that air flow entering TLV #4 near the surface originated near the surface and entered the vortex from all sides, whereas air flow entering the vortex at 1 km AGL originated principally in the RFD. Our results contrast with those of Dahl et al. (2012), who found in idealized simulations that trajectories entering a simulated vortex near the surface originated almost exclusively from the RFD, whereas those entering the low-level mesocyclone from the inflow sector were drawn upwards over the gust front and their associated vorticity ultimately augmented the low-level mesocyclone. Our analyses were of a real case and included the assimilation of volumetric radar data, albeit only from one radar on the 250 m grid (SR1). (An additional experiment in which SR2 data were also assimilated produced similar results, not shown.) Because the storm motion was slow ( $5$  to  $6$   $\text{m s}^{-1}$ ), we do not think that translation of the simulated storm was a significant source of error. Sensitivity of the trajectories to the choice of microphysical parameterization scheme (Dawson et al. 2010), which might influence the downdraft speeds and cold pool strength in the forecast cycles, was not

investigated here. Although our findings should be considered tentative principally for this reason, they merit further examination. We also await similar trajectory analyses in unambiguously tornadic supercells.

## 6. Verification using SR2 data

SR2 was deployed 40 km west of SR1, in order to facilitate dual-Doppler analysis of the Prospect Valley storm. SR1 and SR2 viewed the Prospect Valley storm from roughly perpendicular angles, and therefore each radar sampled a significant component of the other's cross beam flow. Synchronized volumes (intended for dual-Doppler analysis) were collected every three minutes. While volume coverage patterns (VCPs) for SR1 were identical for all but one of the volumes collected from 2227-2327 UTC, those for SR2 changed every few volumes, and were shallower than those from SR2, with more sweeps collected in the boundary layer (Fig. 8). (The VCP was selected by each radar's operator.)

Because of inconsistent SR2 coverage, we elected to run two experiments on the 250 m grid, one in which we assimilated only SR1 data (**250m\_SR1**; described previously), and a second in which we assimilated both SR1 and SR2 data (**250m\_SR1SR2**). Three SR2 volumes (starting at 2233, 2236, and 2239 UTC) contained only low-level single-elevation scans. Full volumes were not available at these times, and because these scans exhibited beam blockage contamination, they were not assimilated.

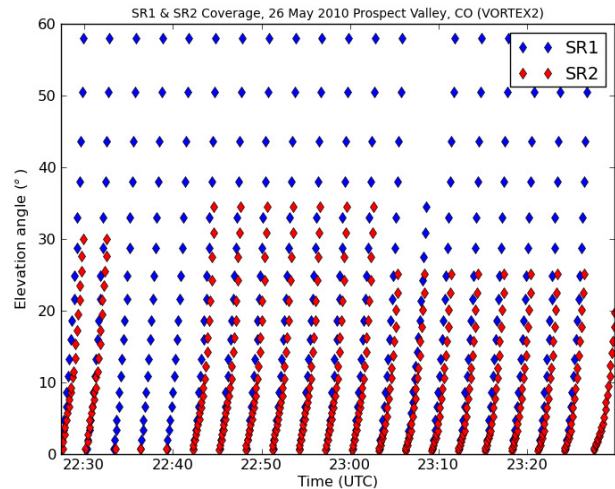


Fig. 8. VCPs for SR1 (blue) and SR2 (red).

Qualitatively, the results from the 250m\_SR1SR2 experiments (not shown) are quite similar to those from 250m\_SR1, with similar evolution of the supercell's hook echo, downdraft pulses, and vorticity maxima. (The precise timing and details of these features will be explored in further studies.) However, the domain-averaged root mean squared innovation (RMSI) and ensemble spread statistics are quite different.

We verified the prior ensemble states (converted into observation space) against  $V_r$  observations from SR1, SR2, and KFTG, all of which had volumetric coverage of the Prospect Valley storm (Fig. 9). Both ensembles exhibited underdispersion at most times; additional measures (such as increasing additive noise or the assumed observation error)

may be needed to increase ensemble spread in future versions of these experiments. (Recall that we assumed observation error of  $2 \text{ m s}^{-1}$  for  $V_r$ .)

Overall, the RMSI and spread statistics for both experiments were similar when verified against SR1 observations. When verified against SR2 observations, the innovations and spread were much smaller in 250m\_SR1SR2 than 250m\_SR1, largely on account of the greater number of observations assimilated. RMSI was nearly halved in the first cycle in which SR2 data were assimilated, indicating faster convergence of the ensemble to a state consistent with SR2 observations. The reduction in the analysis RMSI carried through the 3 min forecasts. When full SR2 volumes were not available for assimilation (2233-2242 UTC), the RMSI and spread increased until they were comparable to those from the 250m\_SR1 experiment. In other words, the improvements to RMSI resulting from assimilation of SR2 data “wore off” after only three assimilation cycles (or about 10 min).

When verified against KFTG data (which were *not* assimilated on the 250 m grid), RMSI in experiment 250m\_SR1SR2 improved slightly over that from 250m\_SR1, leading us to infer that the additional assimilation of SR2 data improved the analyses of the supercell as early as the first assimilation cycle. Our results are consistent with those of Snook et al. (2011), who demonstrated improvement in analyses of a tornadic mesoscale convective system over Oklahoma when assimilating data from multiple closely spaced, short-range, stationary radars in addition to the nearest WSR-88D, and of Tanamachi et al. (2012), who demonstrated similar qualitative improvement in analyses of a tornadic supercell when mobile radar data were assimilated. For the Prospect Valley storm, we expect that the assimilation of data from additional radars, particularly low-altitude observations, would result in further improvement to the analyses; we will attempt to do so in the near future.

## 6. Conclusions

Using the ARPS EnKF data assimilation system, we successfully assimilated mobile radar data on a 250 m grid, generating high spatial resolution analyses of a weakly tornadic supercell every 3 min. The 250 m grid was nested within two coarser-resolution grids on which operational WSR-88D data were assimilated using EnKF. The analyses contained multiple DRCs and accompanying RFD surges, leading us to speculate that these processes may have played an important role in the formation of TLVs near the tip of the hook echo. From trajectory analyses, we determined that air entering the TLVs at 1 km AGL originated principally in the RFD, while air flow entering closer to the surface originated near the surface and entered from all sides. We verified the analyses produced in experiments 250m\_SR1 and 250m\_SR1SR2 by generating synthetic Doppler velocity observations from the model state to match radar VCPs. We found that the assimilation of data from both SMART-Rs decreased both the innovation and spread when verified against independently collected  $V_r$  observations from KFTG. The innovation improvements diminished quickly during a roughly 10 min long gap in SR2 data. It is therefore recommended that, in future field campaigns collecting mobile Doppler radar data for the purpose of data assimilation, special efforts be made to collect synchronized volumes and minimize gaps in volumetric coverage.

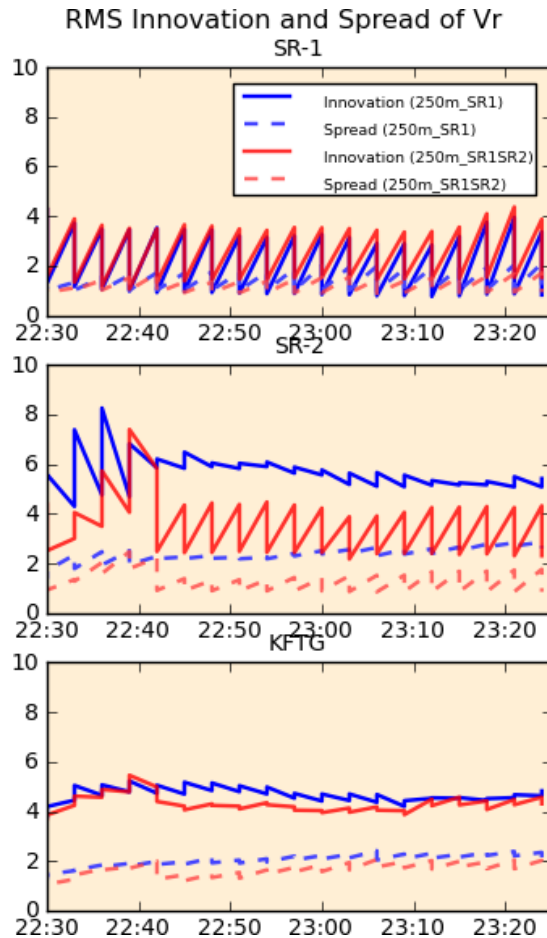


Fig. 9 Innovation (solid lines) and spread (dashed lines) in  $\text{m s}^{-1}$  for experiments 250m\_SR1 (blue) and 250m\_SR1SR2 (red).

## Acknowledgments

This research was supported by National Science Foundation (NSF) grants AGS-0802888, AGS-0637148, and AGS-0934307. Drs. Daniel Dawson, Yunheng Wang, and Nathan Snook instructed the first author in the use of ARPS and ARPSEnKF. Scott Hill provided computing support. Simulations were conducted using the supercomputing resources of the Oklahoma Supercomputing Center for Education and Research (OSCER), under the directorship of Dr. Henry Neeman. WSR-88D data were obtained from the U.S. National Climatic Data Center (NCDC). Gordon Carrie provided the SMART-R data. Additional data were furnished by NCAR/EOL (<http://data.eol.ucar.edu/>), under sponsorship of NSF. NWS warnings and storm reports were retrieved from the Iowa Environmental Mesonet (<http://mesonet.agron.iastate.edu/wx/afos/list.phtml>).

## References

- Anderson, J. L., 2001: An ensemble adjustment Kalman filter for data assimilation. *Mon. Wea. Rev.*, **129**, 2884-2903.
- Biggerstaff, M. I., L. J. Wicker, J. Guynes, C. Ziegler, J. M. Straka, E. N. Rasmussen, A. Doggett, L. D. Carey, J. L. Schroeder, and C. Weiss, 2005: The Shared Mobile Atmospheric Research and Teaching Radar: A collaboration to enhance research and teaching. *Bull. Amer. Meteor. Soc.*, **86**, 1263-1274.
- Caya, A., J. Sun, and C. Snyder, 2005: A comparison between the 4DVAR and the ensemble Kalman filter techniques for radar data assimilation. *Mon. Wea. Rev.*, **133**, 3081-3094.
- Dahl, J. M. L., M. D. Parker, and L. J. Wicker, 2012: Uncertainties in trajectory calculations within near-surface mesocyclones of simulated supercells. *Mon. Wea. Rev.*, accepted.
- Dawson, D. T., M. Xue, J. A. Milbrandt, and M. K. Yau, 2010: Comparison of evaporation and cold pool development between single-moment and multimoment bulk microphysics schemes in idealized simulations of tornadic thunderstorms. *Mon. Wea. Rev.*, **138**, 1152-1171.
- Hayden, C. M., and R. J. Purser, 1995: Recursive filter objective analysis of meteorological fields: Applications to NESDIS operational processing. *J. Appl. Meteor.*, **34**, 3-15.
- Jung, Y., M. Xue, and M. Tong, 2012: Ensemble Kalman filter analyses of the 29-30 May 2004 Oklahoma tornadic thunderstorm using one- and two-moment bulk microphysics schemes, with verification against polarimetric radar data. *Mon. Wea. Rev.*, **140**, 1457-1475.
- Marquis, J., Y. Richardson, P. M. Markowski, D. C. Dowell, J. Wurman, K. Kosiba, and P. Robinson, 2010: Preliminary analysis of the Goshen County tornadic supercell on 5 June 2009 during VORTEX2 using EnKF assimilation of mobile radar and mesonet data. *25th Conf. on Severe Local Storms*, Denver, Colorado, American Meteorological Society, 6.7.
- Rasmussen, E. N., J. M. Straka, M. S. Gilmore, and R. Davies-Jones, 2006: A preliminary survey of rear-flank descending reflectivity cores in supercell storms. *Wea. Forecasting*, **21**, 923-938.
- Snook, N. A., M. Xue, and Y. Jung, 2011: Analysis of a tornadic mesoscale convective vortex assimilating CASA X-band and WSR-88D radar data using an ensemble Kalman filter. *Mon. Wea. Rev.*, **139**, 3446-3468.
- Stensrud, D. J., and J. Gao, 2010: Importance of horizontally inhomogeneous environmental initial conditions to ensemble storm-scale radar data assimilation and very short-range forecasts. *Mon. Wea. Rev.*, **138**, 1250-1272.
- Tanamachi, R. L., L. J. Wicker, D. C. Dowell, H. B. Bluestein, and M. Xue, 2012: EnKF assimilation of high-resolution, mobile Doppler radar data of the 4 May 2007 Greensburg, Kansas supercell into a numerical cloud model. *Mon. Wea. Rev.*, conditionally accepted.
- Tong, M., and M. Xue, 2005: Ensemble Kalman filter assimilation of Doppler radar data with a compressible nonhydrostatic model: OSS experiments. *Mon. Wea. Rev.*, **133**, 1789-1807.
- Wurman, J., L. J. Wicker, Y. P. Richardson, E. N. Rasmussen, P. M. Markowski, D. C. Dowell, D. B. Burgess, and H. B. Bluestein, 2010: An overview of the VORTEX2 field campaign. *25th Conf. on Severe Local Storms*, Denver, CO, American Meteorological Society, 5.1.
- Xue, M., K. K. Droegemeier, and V. Wong, 2000: The Advanced Regional Prediction System (ARPS) – A multi-scale nonhydrostatic atmospheric simulation and prediction model. Part I: Model dynamics and verification. *Meteor. Atmos. Phys.*, **75**, 161-193.
- Xue, M., M. Tong, and K. K. Droegemeier, 2006: An OSSE framework based on the ensemble square root Kalman filter for evaluating the impact of data from radar networks on thunderstorm analysis and forecasting. *J. Atmos. Oceanic Technol.*, **23**, 46-66.